

See discussions, stats, and author profiles for this publication at: <https://www.researchgate.net/publication/46217651>

Ethanol Hydrates and Solid Solution Formed by Gas Condensation: An in Situ Study by Micro-Raman Scattering and X-ray Diffraction

ARTICLE *in* THE JOURNAL OF PHYSICAL CHEMISTRY A · OCTOBER 2010

Impact Factor: 2.69 · DOI: 10.1021/jp101440y · Source: PubMed

CITATION

1

READS

25

3 AUTHORS:



Sébastien Facq

University of Cambridge

10 PUBLICATIONS 66 CITATIONS

SEE PROFILE



Florence Danède

Université des Sciences et Technologies de...

42 PUBLICATIONS 728 CITATIONS

SEE PROFILE



B. Chazallon

Université des Sciences et Technologies de...

54 PUBLICATIONS 702 CITATIONS

SEE PROFILE

Ethanol Hydrates and Solid Solution Formed by Gas Condensation: An in Situ Study by Micro-Raman Scattering and X-ray Diffraction

Sébastien Facq,^{*,†} Florence Danède,[‡] and Bertrand Chazallon^{*,†}

Laboratoire de Physique des Lasers, Atomes et Molécules (PhLAM), Université Lille 1, UMR CNRS 8523, Centre d'Etudes et de Recherches Lasers et Applications (CERLA), 59655 Villeneuve d'Ascq, France, and Unité Matériaux et Transformations, Université Lille 1, UMR CNRS 8207, 59655 Villeneuve d'Ascq, France

Received: February 16, 2010; Revised Manuscript Received: July 12, 2010

Thin films of ethanol–water solid mixtures formed by gas co-condensation are investigated in situ by micro-Raman scattering in the 800–1600 and 2800–3800 cm^{-1} spectral regions. Information at the molecular level on the structure is derived from accompanying changes observed in band shapes and vibrational mode frequencies. Depending on the ethanol content, the formation of two distinct ethanol hydrates is spectroscopically characterized, and their structures are independently confirmed by X-ray diffraction measurements. The attribution of the different phases is made in comparison with literature data and in relation with the ethanol phase diagram. Raman characteristic spectral features of ethanol extremely diluted in ice and corresponding to a solid solution regime are reported.

Introduction

Oxygenated organic species such as light organic compounds (alcohols, ketones, aldehydes, etc.) are found in relatively high abundance^{1,2} in the upper troposphere. Because of their ability to be easily photolyzed, they can provide substantial sources of free OH radicals that are responsible for driving photochemical cycles in the atmosphere that can affect the ozone budget.

Ethanol (EtOH) is known to be abundant in the atmosphere, especially over polluted urban areas due to its use as biofuel or solvents in industry.^{3,4} Moreover, vegetation provides a major source of reactive carbon entering the atmosphere, and it is becoming increasingly clear that a variety of partially oxidized hydrocarbons, principally alcohols (EtOH), is also emitted.⁵

The presence of small ice particles in the troposphere promotes their interactions with atmospheric trace gases. The incorporation of gases at the surface or in the volume of ice can occur via many different trapping processes (adsorption, diffusion, freezing, codeposition; i.e., incorporation of trace gases during growing ice conditions), which can affect both the ice structure and reactivity.^{6,7} This can also modify the gas phase composition and the nature and composition of the incorporated species in ice.

A number of studies have been performed to investigate the adsorption process of a variety of small organic molecules such as EtOH on ice in a temperature range relevant to the troposphere.^{8–10} They used a coated-wall flow tube/mass spectrometer device to determine the adsorption enthalpy of a series of alcohols ($\sim -61 \text{ kJ mol}^{-1}$ for EtOH) and their surface coverages.⁸ The results concerning EtOH were confirmed in a study combining experimental and theoretical calculations.⁹ Furthermore, it was shown recently that the trapped amount of EtOH molecules may be largely increased on supercooled frozen samples doped with nitric acid¹⁰ which is added to limit ice formation and keeps the surface liquid. Although these indirect

instrumental methods may well indicate gas uptake on ice with a high degree of sensitivity, they are unable to give a complete picture of molecular processes occurring at the gas–ice interface. Indeed, the interpretation of the data is usually based on hypothetical models of adsorption that have not always been well calibrated due to a limited characterization and knowledge of the nature of the ice surface and structure.

On the other hand, a number of studies have been performed on the freezing process of the EtOH–water system.^{11–18} They highlight the importance of this system in many fields of chemistry, cryobiology, or astrophysics.¹⁹ They were focused mainly on structural information and the identification of different hydrates in correlation with the ethanol phase diagram using X-ray diffraction, thermal analysis, or dielectric measurements. However, it appears that significant discrepancies still exist in the literature, with uncertainties concerning the composition and the structure of the stable or metastable eutectic or peritectic hydrate phases.^{13,15,16,18}

Recently, a different trapping process was proposed:^{20–22} EtOH–water solid mixtures were formed by co-condensation at low temperature (88 K). The thin films formed were analyzed using micro-Raman spectroscopy. It was suggested that significant differences appear concerning the structural nature of the deposited products with respect to that observed in frozen aqueous solutions.^{20–23} This behavior may be related to the slow dynamic of condensed molecules at low temperature that prevents active clustering processes as those occurring when starting from the liquid. Depending on the initial EtOH gas phase composition, different crystalline phases have been identified during annealing. A modified type I clathrate hydrate (semi-clathrate) of cubic structure (CS-I, space group $Pm\bar{3}n$, $a = 12.006(3) \text{ \AA}$) (hydrate I) was observed at $\sim 143 \text{ K}$ ²¹ with a composition distinct from those reported in the frozen solutions.^{13,18} In clathrates, the EtOH gas molecule (guest) ought to be incorporated selectively into the different cages of the host framework constituted by water molecules. This can generate compounds of variable compositions. During heating at higher

* Corresponding authors. Phone: +33 (0)320336468. Fax: +33 (0)320336463. E-mail: chazallon@phlam.univ-lille1.fr. (S.F.); facq@phlam.univ-lille1.fr (B.C.).

[†] PhLAM.

[‡] Unité Matériaux et Transformations.

temperature, a distinct hydrate (hydrate II) (~ 190 K) whose structure of nonclathrate type remains undetermined²¹ was formed.

In the present study, we report on micro-Raman analysis of different EtOH–water solid mixtures formed by co-condensation at 183 K. The temperature is chosen to account for the conditions observed in the upper troposphere. X-ray measurements are carried out independently to corroborate the structural modifications identified by Raman.

Experimental Section

Materials. The experimental setup and deposition protocol have been described in more detail in a previous paper.²⁰ Briefly, EtOH aqueous solutions of concentration $(X_{\text{EtOH}})_l = 0.05, 0.5, 2, 3, 4, 5, 7$, and 17 mol % are prepared with EtOH purchased from Verbière (France) (purity >99.77%) mixed with double-distilled and -deionized water (resistivity $\sim 18 \text{ M}\Omega/\text{cm}^{-1}$) or deuterium oxide (Aldrich chemistry 99.9 atom % D). Vapor–liquid equilibrium of each aqueous solution is reached in a thermally insulated glass bulb maintained at 294 ± 1 K. The collected EtOH–H₂O vapors are introduced through an in-line membrane valve in a dedicated cryostage (LINKAM) precooled at 183 K and pumped to low pressure. The pressure rapidly increases from a residual value of $\sim 10^{-3}$ Torr to a manually adjusted value of 10^{-1} Torr for all the set of experiments. The vapor mixture condenses onto a silver-coated copper sample holder, and after 30–60 s of deposition, an optimal Raman signal of a thin ice film of typically ~ 150 – $300 \mu\text{m}$ thickness is obtained. The valve is then closed, and the pressure decreases to the residual value in a few seconds. The Raman spectra are then collected at 88 K to highlight weak spectral modifications representative of the structure of samples formed at 183 K.

Micro-Raman Measurements. All spectra are recorded in the 800–1600 and 2800–3800 cm^{-1} spectral regions. We used an InVia Reflex Raman spectroscopy (Renishaw). This highly sensitive spectrometer has a 250 mm focal length and is equipped with an Olympus BXFM free-space microscope on which the cryostage is mounted. A spectral resolution of $\sim 1 \text{ cm}^{-1}$ is reached with a holographic grating of 1800 grooves/mm and a Peltier cooled front illuminated CCD detector (576×400 pixels). The excitation radiation ($\lambda = 514.5 \text{ nm}$) is produced by an Ar laser source (Coherent). An Olympus 50 \times objective (0.5 N.A.) provides an $\sim 1 \mu\text{m}$ circular beam spot. The laser power at sample is 3–4 mW as measured by a Lasercheck powermeter (Coherent). Spectral positions were calibrated against the silicon line, yielding a stable value of $520.4 \pm 0.3 \text{ cm}^{-1}$. All spectra are baseline-corrected, and the peak positions of the collected spectra were determined using a least-squares fitting procedure. Spectra of samples formed at 88 K were recorded with a X-Y DILOR spectroscopy and present a lower signal/noise ratio.

X-ray Measurements. X-ray diffraction measurements are performed using an X-pert pro MPD powder diffractometer ($\lambda_{\text{CuK}\alpha} = 1.54059 \text{ \AA}$) (PANalytical) upgraded with the X'Celerator detector (PANalytical), providing high-speed powder XRD measurements. X-rays are generated by a high-energy ceramic sealed tube (1.8 kW) operated at 45 kV and 40 mA. The sample stage consists of a modified Anton-Paar TTK 450 cryostat (80–723 K), allowing the gas introduction through a membrane valve. Bragg reflections are indexed and refined using the EXPO 2004 software.²⁴

Results and Discussion

Ice Film Composition. Gaseous mixtures of water and ethanol of compositions $Y_{\text{EtOH}} = 0.52, 4.87, 16.4, 22.2, 27.1$,

TABLE 1: Experimental Ethanol–Water Mixtures of Different Compositions^a

$(X_{\text{EtOH}})_l$ aqueous solutions (mol %)	Y_{EtOH} calculated gas phase (mol %)	$(X_{\text{EtOH}})_s$ calculated condensed phase (mol %)
0.05 ^b	0.5	0.3
0.5 ^b	4.9	3.1
0.6 ^c	5.8	3.7
1.9 ^c	15.7	10.4
2 ^b	16.4	10.9
3 ^b	22.2	15.1
4 ^b	27.1	18.8
4.5 ^c	29.2	20.5
5 ^b	31.1	22
7 ^b	37.6	27.3
8.9 ^c	42.3	31.4
17 ^{b,c}	54.2	42.5

^a The equilibrium gas phase composition (Y_{EtOH}) above solutions of different concentrations $(X_{\text{EtOH}})_l$ is derived from the Wilson model.²⁵ The condensed phase composition $(X_{\text{EtOH}})_s$ is calculated according to the condensation model (see text). ^b Sample analyzed by micro-Raman spectroscopy (this work). ^c Sample analyzed by micro-Raman spectroscopy (previous work)^{20,21}

31.1, 37.6, and 54.2 mol % are collected at equilibrium above ethanol aqueous solutions of compositions $(X_{\text{EtOH}})_l = 0.05, 0.5, 2, 3, 4, 5, 7$, and 17 mol %, respectively. The gas phase composition is determined from the thermodynamic model developed by Wilson²⁵ that was proven to have a very high accuracy²⁶ for numerous multicomponent systems, including alcohol–water systems. The ice film composition is estimated from a kinetics law²⁰ that determines the ethanol concentration in the solid $(X_{\text{EtOH}})_s$,

$$(X_{\text{EtOH}})_s = \left(1 + \frac{P_{\text{EtOH}} \cdot \alpha_{\text{EtOH}}}{P_{\text{H}_2\text{O}} \cdot \text{H}_2\text{O}} \cdot \sqrt{\frac{M_{\text{H}_2\text{O}}}{M_{\text{EtOH}}}} \right)^{-1} \quad (1)$$

where P_i is the partial pressure of the component i before deposition, α_i is the mass accommodation coefficient (assumed to be close to that of water at 183 K²⁷ for the calculations presented in Table 1), and M_i is the molar mass. The ice film solid phase composition is calculated using both eq 1 and the predicted gas phase composition. All these results are summarized in Table 1.

In the following, $(X_{\text{EtOH}})_s$ will be considered as the initial composition of the deposits. It is assumed that $(X_{\text{EtOH}})_s$ could vary after hydrate formation.

Aqueous solutions of ethanol. To have a better picture on structural changes occurring in the codeposits, we first briefly investigate the situation in the liquid to obtain reference data. The Raman spectra of ethanol aqueous solutions show three main bands located at ~ 2877 , ~ 2929 , and $\sim 2974 \text{ cm}^{-1}$. The assignment of the vibrational spectrum of liquid and solid ethanol was originally proposed by Perchard and Josien^{28,29} (1968) using the IR and Raman measurements of 12 isotopic species of ethanol. They assigned the first band to the symmetric stretching mode of $-\text{CH}_2$ group and the two others to the symmetric and antisymmetric stretching modes of $-\text{CH}_3$ group, respectively. Nevertheless, recent papers^{30,31} put this assignment into question. Yu et al.,³¹ (2007) have applied polarized photoacoustic Raman spectroscopy (PARS) and density functional theory calculations at the B3LYP/6-311G(d,p) level to assign the vibrational spectra of gaseous and liquid $\text{CH}_3\text{CH}_2\text{OH}$, $\text{CH}_3\text{CD}_2\text{OH}$, and $\text{CD}_3\text{CH}_2\text{OH}$. They suggest that Fermi resonance coupling exists between the first overtones of the bending

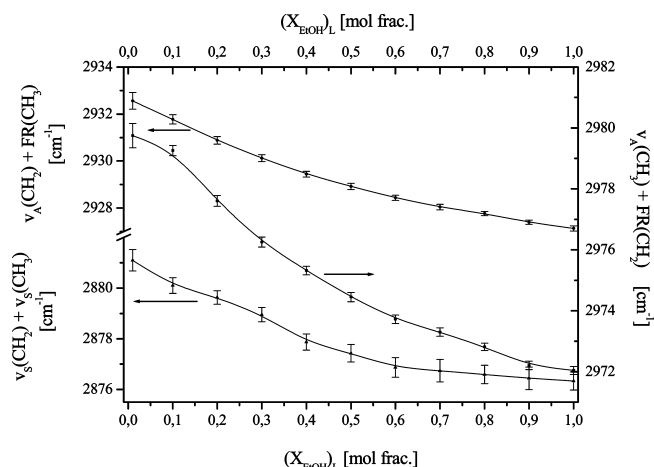


Figure 1. Evolution of the ethanol C–H stretching mode frequencies as a function of concentration in aqueous solutions: $(X_{\text{EtOH}})_L$. The attribution of the bands to the different modes is based on earlier work.³¹

vibrational modes of both $-\text{CH}_2$ and $-\text{CH}_3$ groups and their respective fundamental C–H symmetric stretching modes.

According to Yu et al.,³¹ the band at $\sim 2877 \text{ cm}^{-1}$ was ascribed to the overlapping symmetric stretching vibrational modes of both $-\text{CH}_2$ and $-\text{CH}_3$ [$\nu_s(\text{CH}_3)$ and $\nu_s(\text{CH}_2)$], the band at $\sim 2929 \text{ cm}^{-1}$ was assigned to the two symmetric $-\text{CH}_3$ Fermi resonance modes and the weak $-\text{CH}_2$ antisymmetric stretching mode [$\nu_A(\text{CH}_2)$ and $\text{FR}(\text{CH}_3)$], and the band at $\sim 2974 \text{ cm}^{-1}$ was assigned to the symmetric $-\text{CH}_2$ Fermi resonance mode and the weak $-\text{CH}_3$ antisymmetric stretching mode [$\nu_A(\text{CH}_3)$ and $\text{FR}(\text{CH}_2)$]. In this paper, we follow the same assignment for our solid mixtures.

In Raman spectra of EtOH aqueous solutions, all C–H stretching bands shift to lower frequencies as $(X_{\text{EtOH}})_L$ increases (see Figure 1). As described elsewhere,³² this red shift may be explained by a partial and gradual electron transfer from the hydrogens and carbon to the oxygen of the EtOH molecule to participate in H-bond formation. This view is consistent with the gradual increase with concentration of the H-bond strengths of the EtOH molecules.

Vapor Deposited Ethanol–Water Mixtures.

C–H Vibrational Mode Spectral Region. Raman spectra of EtOH– H_2O solid mixtures at $(X_{\text{EtOH}})_s$ of 0.3, 3.1, 10.9, 15.1, 18.8, 22, 27.3, and 42.5 mol % formed at 183 K are recorded in the C–H vibrational mode spectral region $2800\text{--}3800 \text{ cm}^{-1}$ and plotted as a function of $(X_{\text{EtOH}})_s$ in Figure 2A. For comparison, EtOH solid mixtures of similar concentrations but formed at 88 K are displayed in Figure 2B).

We will focus here on the characteristic spectral changes observed between EtOH– H_2O vapor mixtures codeposited at 183 and 88 K. At 88 K, the molecules are frozen in random orientations^{20,21} and the Raman spectra exhibit weak and broad bands that are characteristic spectral features of an amorphous solid.

Important differences in band positions, shapes, and bandwidths emerge when the samples are formed at 183 K. The C–H bands are more intense and sharper. For example, the full width at half-maximum (fwhm) of the main C–H band at $\sim 2929 \text{ cm}^{-1}$ is about $\sim 11 \text{ cm}^{-1}$ for the 183 K samples versus $\sim 23 \text{ cm}^{-1}$ for the 88 K samples. Only the 183 K sample with EtOH content of $(X_{\text{EtOH}})_s = 42.5 \text{ mol } \%$ escapes this rule, with a fwhm close to $\sim 23 \text{ cm}^{-1}$ (Figure 2(A)). Further, it can be seen that all deposits show a red shift of $\sim 3 \text{ cm}^{-1}$ at 183 K in comparison with the 88 K samples, and the absolute C–H band position is

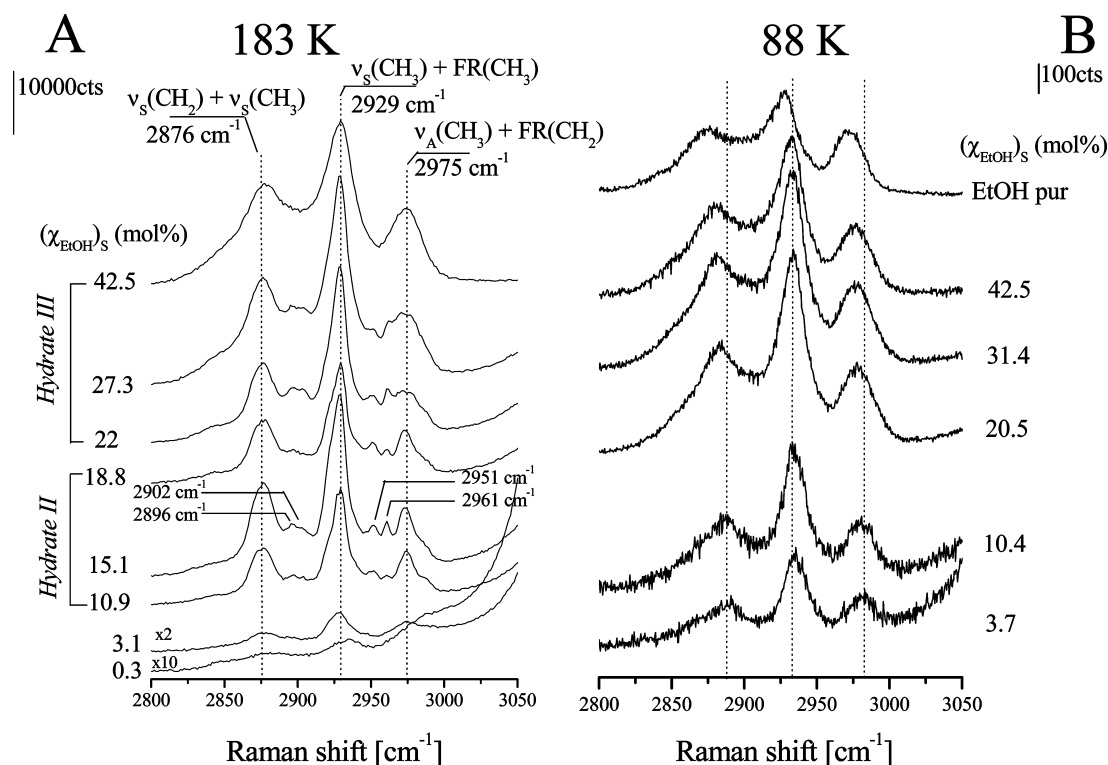


Figure 2. Raman spectra, recorded in the $2800\text{--}3800 \text{ cm}^{-1}$ spectral region, of different EtOH– H_2O mixtures deposited at 183 (A) and 88 K (B). Concentrations are given for the different solid films. Vertical dotted lines indicate the approximate band positions of the main C–H stretching modes of ethanol. The attribution of the bands to the different modes is based on earlier work.³¹ The difference in spectral features corresponds to different hydrate structures and concentration regimes (see text). Note the differences of the bandwidths and band structures between spectra of 183 K samples and 88 K samples (see discussion).

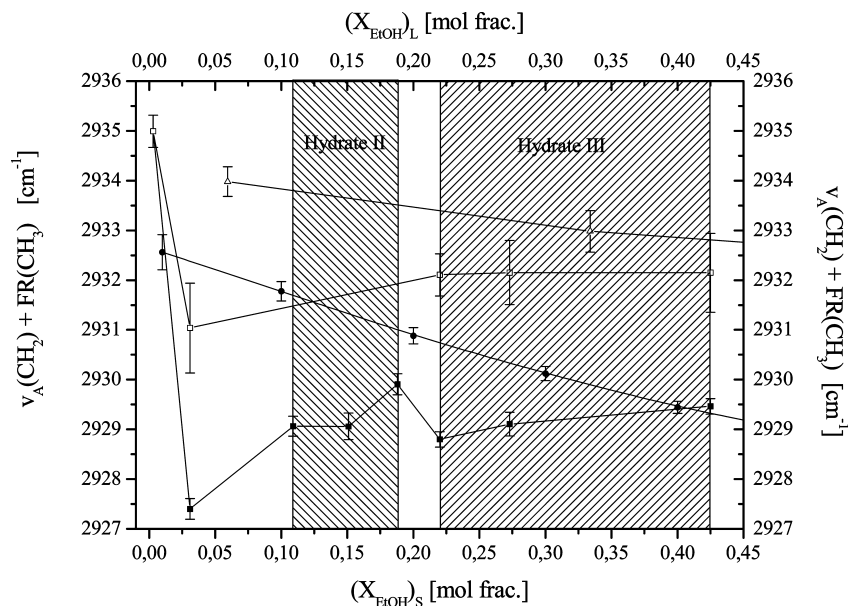


Figure 3. Evolution of the main C–H band of ethanol as a function of the concentration of ethanol in the film ($(X_{\text{EtOH}})_s$) for EtOH–H₂O vapor mixtures codeposited at 183 K (solid squares), EtOH–D₂O vapor mixtures codeposited at 183 K (open squares), and EtOH–H₂O vapor mixtures codeposited at 88 K (open triangles). The evolution of the main C–H band of ethanol in aqueous solutions as a function of concentration ($(X_{\text{EtOH}})_s$) is shown for comparison (solid circles).

the lowest for the 183 K samples (Figure 3). This is an indication for crystallization and for a strengthening of the H-bonds in comparison with the amorphous solid state. As confirmed by our X-ray diffraction work, the 183 K samples form directly crystalline structures (see below).

We do not observe significant deviations of the C–H band position in the range $(X_{\text{EtOH}})_s = 10.9\text{--}42$ mol % for the 183 K samples, except between 15 and 22 mol %. As observed by X-rays, a structural rearrangement around EtOH molecules is found at ~ 22 mol %, with the formation of a distinct crystalline structure (see below). Furthermore, at $(X_{\text{EtOH}})_s = 3.1$ mol %, the molecular spectra indicate a possible change of structure as revealed by the important red shift of the C–H band relative to the liquid. Further work by X-ray diffraction is needed to elucidate this finding.

Additional information can be gained from the weak spectral components appearing in the C–H vibrational mode spectral region for $10.9 \text{ mol } \% \leq (X_{\text{EtOH}})_s \leq 18.8 \text{ mol } \%$. They are located at ~ 2896 , ~ 2902 , ~ 2951 , and $\sim 2961 \text{ cm}^{-1}$ (Figure 2A). Their occurrence may well correspond to the interaction of the water molecule with the hydrogen atoms of the ethanol methyl group. In support of this, previous papers^{33,34} have recently suggested that a C–H group could act as a proton donor in a C–H \cdots O hydrogen bond. Moreover, Oliveira et al.³⁵ have identified new interactions existing between the water molecule and the hydrogen atoms of the methyl groups in both ethanol–water and *t*-butanol–water hydrogen complexes. Their results show that the water molecule simultaneously interacts with the hydroxyl group and with the methyl group in the ethanol and *t*-butanol, respectively. Because the number of water molecules surrounding the ethanol is high at low concentration, the number of C–H \cdots O H-bonds becomes important³⁶ and contributes significantly to the spectra. The C–H bond lengths and the H–C–H angles of the methyl group and the ethyl group could be perturbed by this interaction. This can result in a lowering of the symmetry of the vibration of both methyl group and ethyl group. This loss of symmetry entails a level splitting of the vibrational states of the $[\nu_A(\text{CH}_3)]$ and $[\text{FR}(\text{CH}_2)]$ band into independent contributions (~ 2896 , ~ 2902 , ~ 2951 , and

$\sim 2961 \text{ cm}^{-1}$, Figure 2A). The same behavior is expected for the $[\nu_A(\text{CH}_2)]$ and $[\text{FR}(\text{CH}_3)]$ and $[\nu_S(\text{CH}_3)]$ and $[\nu_S(\text{CH}_2)]$ bands, indicating that all the hydrogens participate in the formation of C–H \cdots O H-bonds.

On this basis, one may expect that EtOH–H₂O solid mixtures of $10.9 \text{ mol } \% \leq (X_{\text{EtOH}})_s \leq 18.8 \text{ mol } \%$ crystallize directly during the deposit at 183 K in an EtOH hydrate structure. This is corroborated by our diffraction experiments carried out in the same concentration range and the identification of the hydrate II. In contrast, this band splitting is not observed for samples codeposited at 88 K at similar concentrations. The amorphous solid state does not present any long-range order, and the contribution to the C–H spectral vibration is averaged over a broad distribution of C–H bond lengths and H–C–H angles.

Beyond $(X_{\text{EtOH}})_s \geq 22 \text{ mol } \%$, the additional spectral components mentioned above gradually disappear, and all main C–H bands broaden. Because the number of water molecules surrounding ethanol is reduced, the spectral contribution of the C–H \cdots O H-bond is weak and does not perturb the C–H spectral region significantly. The symmetry of the vibration is probably close to the C_{3v} point group, as for pure EtOH. These spectral modifications imply a structural reorganization and the formation of a distinct hydrate. This is confirmed by our X-ray diffraction work with the identification of a new hydrate (hydrate III, see below).

At low concentration, the Raman spectrum of the $(X_{\text{EtOH}})_s = 3.1 \text{ mol } \%$ shows weak but noticeable changes in comparison with the spectra representative of the EtOH hydrate II. The weak lines characteristic of EtOH–hydrate II reported above disappear, and modifications appear in the C–O vibrational mode spectral region (see below). Therefore, we cannot exclude the formation of a distinct hydrate at $(X_{\text{EtOH}})_s = 3.1 \text{ mol } \%$. Further work is needed to elucidate this finding.

The situation of the EtOH–H₂O solid mixture of $(X_{\text{EtOH}})_s = 0.3 \text{ mol } \%$ is unique. The intense symmetric O–H stretching mode of water overlaps the EtOH C–H stretching contributions and hinders a clear assignment. By substituting water with deuterium oxide, we gain better insights on the spectral features in the C–H region. The spectra presented in Figure 4 show

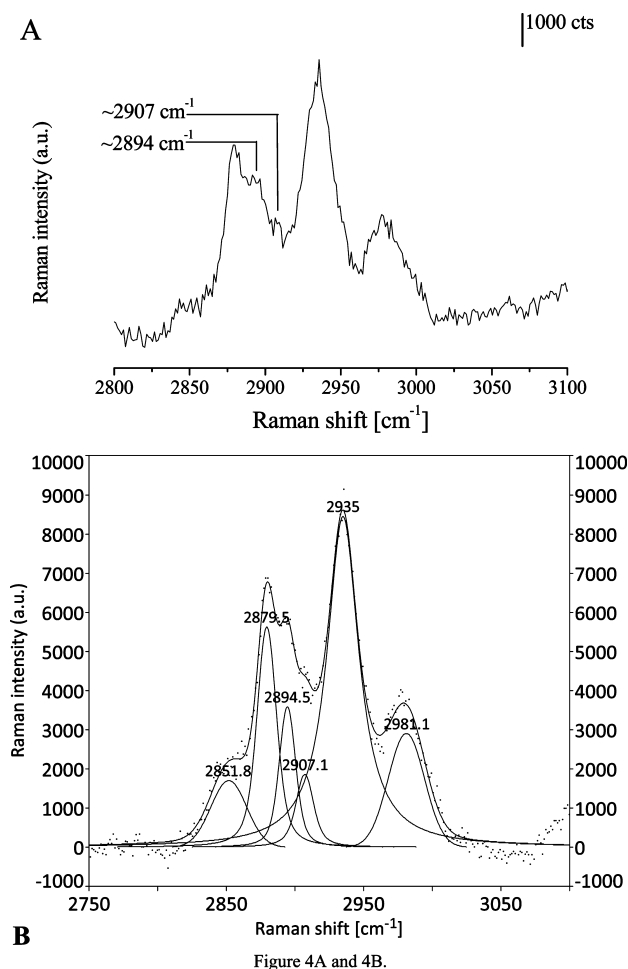


Figure 4. Raman spectra recorded in the 2800–3800 cm^{-1} spectral region of vapor-deposited EtOH–D₂O mixtures ($(X_{\text{EtOH}})_s = 0.3 \text{ mol } \%$) at 183 K (A) and the corresponding spectra with spectral deconvolution using a least-squares protocol (B). Note the occurrence of spectral components on the high-frequency side of the band at 2879 cm^{-1} . Their presence characterizes the formation of a distinct phase (see text).

additional components located at ~ 2894 and $\sim 2907 \text{ cm}^{-1}$ that have grown on the high frequency side of the C–H band [$\nu_s(\text{CH}_3)$ and $\nu_s(\text{CH}_2)$] at $\sim 2879 \text{ cm}^{-1}$.

Furthermore, the position of the main band [$\nu_A(\text{CH}_2)$ and $\text{FR}(\text{CH}_3)$] shows a significant shift ($\sim 7.5 \text{ cm}^{-1}$) to higher wavenumbers relative to that of samples with a higher EtOH content. Even if this effect can partly be attributed to the isotopic substitution, it certainly reflects a change in the molecular structure of the deposit. Different EtOH–D₂O solid mixtures at $(X_{\text{EtOH}})_s = 3.1, 22, 27.3$, and $42.5 \text{ mol } \%$ were prepared for comparison. The C–H band position [$\nu_A(\text{CH}_2)$ and $\text{FR}(\text{CH}_3)$] of the deuterated samples presents a blue shift of $\sim 3 \text{ cm}^{-1}$ relative to the hydrogenated ones (Figure 3). This is attributed to a shortening of H-bonds in EtOH–D₂O solid mixtures. Thus, the remarkable drop in frequency observed at low concentration with $(X_{\text{EtOH}})_s = 0.3 \text{ mol } \%$ cannot be ascribed to only the isotopic substitution effect. We suggest, therefore, that the drop in frequency is a spectral feature of doped ice samples with EtOH molecules extremely diluted in the network.

C–O Vibrational Mode Spectral Region. As shown in Figure 5, the C–O vibrational mode spectral region exhibits subtle spectral changes that indicate modifications of the structure as the EtOH content is changed.

The band $\nu_s(\text{CCO})$ at $\sim 882 \text{ cm}^{-1}$ ^{28,29} is split into spectral components located at ~ 875 and $\sim 886 \text{ cm}^{-1}$ with a fwhm (875

cm^{-1}) $\sim 11 \text{ cm}^{-1}$ and fwhm (886 cm^{-1}) $\sim 8.5 \text{ cm}^{-1}$ as $10.9 \text{ mol } \%$ $\leq (X_{\text{EtOH}})_s \leq 18.8 \text{ mol } \%$. In contrast, above $(X_{\text{EtOH}})_s = 22 \text{ mol } \%$, the $\nu_s(\text{CCO})$ band broadens with a fwhm of $\sim 15 \text{ cm}^{-1}$ and becomes asymmetric. These changes are accompanied by a change in the integrated intensity ratio of the bands at $\sim 1051 \text{ cm}^{-1}$ and $\sim 1093 \text{ cm}^{-1}$ ($I_{1051 \text{ cm}^{-1}}/I_{1093 \text{ cm}^{-1}}$). For example, $1.1 \leq I_{1051 \text{ cm}^{-1}}/I_{1093 \text{ cm}^{-1}} \leq 1.4$ for $10.9 \text{ mol } \%$ $\leq (X_{\text{EtOH}})_s \leq 18.8 \text{ mol } \%$, whereas $I_{1051 \text{ cm}^{-1}}/I_{1093 \text{ cm}^{-1}} = 1$ for $(X_{\text{EtOH}})_s \geq 22 \text{ mol } \%$. This reflects an increasing contribution of the hydrogens from CH₃ rocking and an end-group C–OH bending due to different hydrogen bonding in this structure.

At low EtOH content ($(X_{\text{EtOH}})_s = 3.1 \text{ mol } \%$), the $\nu_s(\text{CCO})$ band at 879 cm^{-1} becomes broad, with a fwhm $\sim 17.5 \text{ cm}^{-1}$. This supports the previous conclusion concerning the C–H bands and a modification of the structure distinct from that of hydrate II. Additional insights into the structural change have been gained from X-ray diffraction using the same experimental conditions.

Hydrate Structures of the 88 K Deposits. In Figure 6, we plot typical diffraction patterns collected during annealing of a thin film codeposited at 88 K of an EtOH–H₂O gas mixture of composition $\sim 42 \text{ mol } \%$ ($(X_{\text{EtOH}})_s = 31.4 \text{ mol } \%$). The broad background scattering present at 88 K indicates that the film is amorphous at low temperature (up to $T \leq 128 \text{ K}$). The deposit undergoes successive structural changes as the temperature is increased at 5 K min^{-1} . This leads to the formation of a hydrate I (actually a modified type I clathrate (CS-I)) at 143 K ²¹ and a crystalline hydrate II at 193 K ²¹. Depending on the EtOH content, the hydrate I is formed in the ~ 130 – 163 K temperature range, whereas the hydrate II phase is found at $\sim 158 \text{ K}$ or in the 188 – 198 K temperature range. Bragg reflexes of the clathrate types I and II are shown in Figure 6 to highlight the fact that distinct structures are formed in our deposits.

Hydrate Structures of the 183 K Deposits. Diffraction patterns of deposits of compositions $(X_{\text{EtOH}})_s = 3.1, 18.8, 22, 27.3$, and $42.5 \text{ mol } \%$ have been recorded. Typical results are presented in Figure 7 for EtOH–H₂O solid mixtures of $(X_{\text{EtOH}})_s = 18.8 \text{ mol } \%$ (hydrate II, see below) and $(X_{\text{EtOH}})_s = 42.5 \text{ mol } \%$ (hydrate III, see below). For comparison, the diffraction pattern of the hydrate I²¹ is also shown in Figure 7. The half-width of the reflexes in the diffraction pattern of hydrate I is larger than that of hydrates II and III. This is explained by the smaller size of crystallites for this hydrate. We estimate the crystallite sizes to be $\sim 511 \text{ \AA}$, according to a full pattern Le Bail refinement and by considering the contribution of the instrument to the peak broadening in the calculation (by using a reference sample (silicon)). The crystallite sizes of hydrates II and III cannot be estimated with a Le Bail refinement because the half-width of the reflexes of their diffraction patterns are comparable to the resolution of the XRD apparatus. They correspond to larger crystallites that have grown faster at relatively higher temperature in comparison with those of the hydrate I.

Diffraction patterns of ice I_h, ice I_c, ethanol RP, and the stable monoclinic crystalline EtOH have been collected for comparison (not shown here). Ice I_h is only present (and preponderant) in deposits of low EtOH content (e.g., $(X_{\text{EtOH}})_s = 3.1 \text{ mol } \%$). In contrast, none of these phases exists at 183 K, and thus, no phase separation takes place when the EtOH content is higher.

All 59 Bragg reflections of the diffraction pattern of the $(X_{\text{EtOH}})_s = 18.8 \text{ mol } \%$ EtOH–H₂O solid mixture may be indexed on the basis of the EtOH hydrate II structure reported earlier²¹ (see Figure 6). Unfortunately, the calculation of the peak indexing procedure does not give results for the crystal

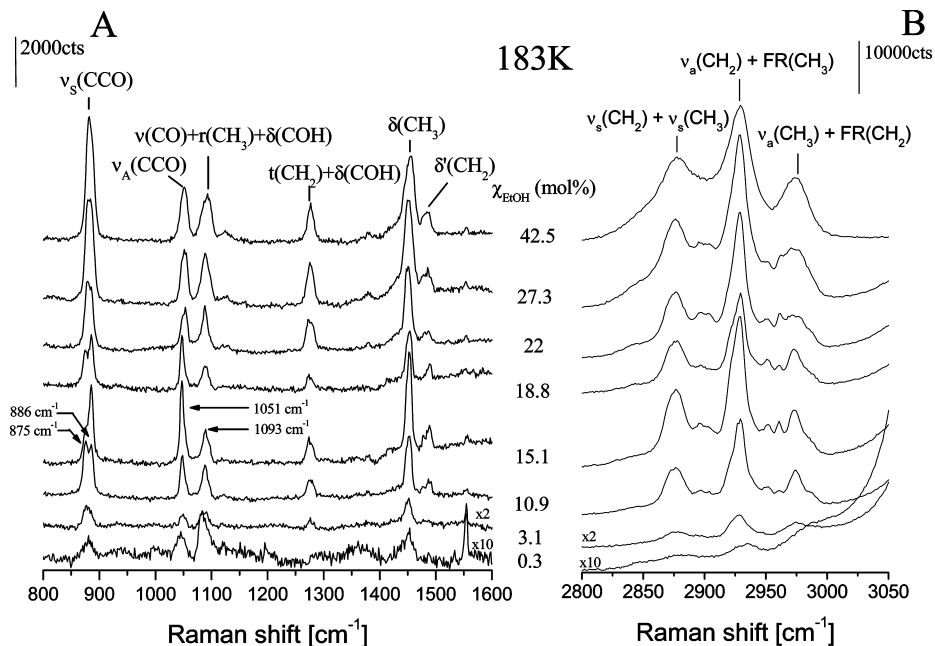


Figure 5. Raman spectra of different EtOH–H₂O mixtures codeposited at 183 K in the C–O vibrational mode spectral region (A) and in the C–H vibrational mode spectral region (B). The attribution of the bands in the (A) panel is based on the work of Perchard and Josien.^{28,29} In the B panel, the attribution is based on an earlier study.³¹ The concentration given corresponds to that estimated in the solid film. The arrows indicate the band splitting of the $\nu_s(\text{CCO})$ symmetric stretching mode as a function of the ethanol content. The bands associated with the change in intensity as a function of ethanol concentration are indicated by arrows at ~ 1051 and ~ 1093 cm^{-1} .

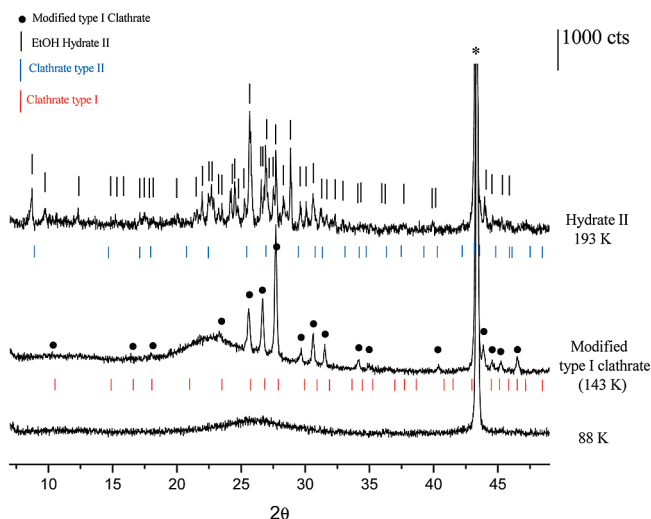


Figure 6. Diffraction patterns (collected with $\lambda_{\text{CuK}\alpha} = 1.540\,59$ Å) of an EtOH–H₂O solid mixture of $(X_{\text{EtOH}})_s = 31.4$ mol % codeposited at 88 K. During annealing, the deposit shows the successive crystallization of two independent ethanol hydrates at 143 K (modified type I clathrate) and 193 K (hydrate II). Solid circles show the Bragg reflections of the modified type I clathrate (hydrate I), and vertical black bars show the Bragg reflections of the hydrate II. Vertical red bars indicate the positions of the Bragg reflections of a clathrate type I, and vertical blue bars indicate the position of the Bragg reflections of a clathrate type II. The asterisk (*) shows a parasitic reflection of the sample holder. The 2θ positions of Bragg reflexes of the Hydrates I, II, and III are given in a table available in the Supporting Information.

pattern of this hydrate. Its structure of low symmetry (not cubic) remains to be determined.

In contrast, diffraction patterns with $(X_{\text{EtOH}})_s \geq 22$ mol % show 11 strong Bragg reflections and weak peaks from hydrate II. A new crystalline EtOH hydrate phase (hydrate III) has formed and is mixed with the ethanol hydrate II. This is in accordance with the Raman results discussed above. The contributions of the EtOH hydrate II phase gradually disappear

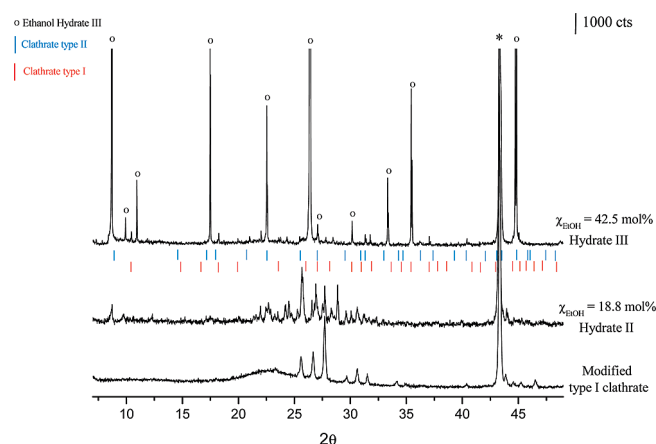


Figure 7. Diffraction patterns (collected with $\lambda_{\text{CuK}\alpha} = 1.540\,59$ Å) of EtOH–H₂O solid mixtures formed at 183 K with a composition in the solid estimated at $(X_{\text{EtOH}})_s = 42.5$ and 18.8 mol %, respectively. They are representative of the distinct ethanol hydrate structures identified in the different concentration ranges. Open circles show the Bragg reflections of the hydrate III. For comparison, vertical red bars indicate the positions of the Bragg reflections of a clathrate type I, vertical blue bars indicate the position of the Bragg reflections of a clathrate type II. The modified type I clathrate from Figure 6 is displayed for comparison. The asterisk (*) shows a parasitic reflection of the sample holder. The 2θ positions of Bragg reflexes of the Hydrates I, II, and III are given in a table available in the Supporting Information.

as the concentration in EtOH is increased. The 11 Bragg reflections observed for the $(X_{\text{EtOH}})_s = 42.5$ mol % sample (Figure 7) have been indexed in terms of the tetragonal $P4/mmm$ space group. The refinement of the cell parameters provides unit cell dimensions of $a = 2.543$ Å and $c = 10.118$ Å. The tetragonal structure (structure-T or ST) of hydrate III is not a common structure for clathrate hydrates that generally crystallize either in cubic (CS-I or CS-II) or hexagonal structure (sH)³⁷ for large guest molecules. However, a tetragonal structure is a common structure of semiclathrates of ammonium salts with, however, much larger cell dimensions.³⁸

Attribution of the Hydrate Structures in Relation to Literature Data. During annealing at 5 K min^{-1} from 183 K, the hydrate II decomposes at about 198 K ($T_d = 198\text{ K}$), and the decomposition of the hydrate III phase occurs at about 208 K ($T_d = 208\text{ K}$).

The decomposition temperature could help in the attribution of the different hydrate phases reported here. Although there are some uncertainties concerning the exact structure of the EtOH hydrates, there is a general consensus that a clathrate CS-II, possibly modified, can exist with a composition close to $\text{EtOH} \cdot 17\text{H}_2\text{O}$.^{11–18} In addition, a potentially modified CS-I structure of composition in the range $\text{EtOH} \cdot (4.75–7.67)\text{H}_2\text{O}$ could form. The occurrence of H-bonds between EtOH and water molecules could strongly distort the lattice and change its symmetry.¹³ Zelenin¹⁶ reviewed the results obtained on this system in the literature (omitting the extensive work of Takaizumi et al.¹⁴) and investigated the $\text{EtOH}–\text{H}_2\text{O}$ phase diagram using differential thermal analysis at atmospheric pressure and pressures up to 10 kbar. It was found that three different ethanol hydrates are present: one stable hydrate of composition $\text{C}_2\text{H}_5\text{OH} \cdot 2\text{H}_2\text{O}$ (*h2*) with $T_d = 208\text{ K}$ and two metastable hydrates of composition $\text{C}_2\text{H}_5\text{OH} \cdot 3\text{H}_2\text{O}$ (*h3*) ($T_d = 204\text{ K}$) and $\text{C}_2\text{H}_5\text{OH} \cdot 4.75\text{H}_2\text{O}$ (*h5*) ($T_d = 198.5\text{ K}$). According to Zelenin,¹⁶ the hydrate of composition $\text{C}_2\text{H}_5\text{OH} \cdot 4.75\text{H}_2\text{O}$ (*h5*) is attributed to a modified CS-I structure obtained by replacing one water molecule with each hydroxyl group of EtOH guest molecules in all the cages. Zelenin's conclusion is based on earlier diffraction results¹³ in which a clathrate CS-I has been identified (lattice of $a = 11.9\text{ Å}$) and seemingly the appropriate stoichiometry. However, the decomposition of this clathrate occurs at $\sim 208\text{ K}$; thus, at higher temperature than that observed by Zelenin (198.5 K). In contrast, the modified clathrate CS-II¹³ ("semiclathrate") decomposes at $\sim 198.5\text{ K}$ with a stoichiometry of $\text{C}_2\text{H}_5\text{OH} \cdot 17\text{H}_2\text{O}$. These inconsistencies lead Zelenin to conclude to the nonexistence of a semiclathrate CS-II.

However, several authors reported the existence of the semiclathrate CS-II in the past.^{12–15} For example, Takaizumi et al.¹⁴ confirmed the formation of many ethanol hydrates in frozen aqueous solutions and classified them into two groups: one derived from the clathrate hydrate CS-I and another from the clathrate hydrate CS-II; that is, with composition varying in the range $\text{C}_2\text{H}_5\text{OH} \cdot (17–4.67)\text{H}_2\text{O}$ (CS-II or CS-I). He found that in the concentration range between 4.2 and 14.4 mol %, there is coexistence of ethanol (semi)clathrates of CS-I and CS-II, alternately CS-II, CS-I and CS-II as (X_{EtOH})_l increases from 0 to 15 mol %. In the lower concentration range, ice I_h first separates from the liquid solution and the semiclathrate CS-II is formed, whereas higher alcohol hydrates first separate in the higher concentration part.

More recently, he studied time-dependent phenomenon in freezing–thawing cycles and suggested the presence of (semi)clathrates CS-I and CS-II at (X_{EtOH})_l > 14.4 mol %.¹⁸ These results suggest a good coincidence between the nature of clusters in their region of stability in the liquid and the structure of hydrate phases in the frozen solid. In summary, Takaizumi et al.,¹⁴ and Takaizumi¹⁸ found consistent results with Boutron and Kaufmann¹³ concerning the existence of a modified CS-II clathrate. Therefore, we believe that Zelenin's attribution is erroneous and that their hydrate of composition $\text{C}_2\text{H}_5\text{OH} \cdot 4.75\text{H}_2\text{O}$ is not a modified CS-I but corresponds to our hydrate II (see below).

The structure of hydrate II observed here is definitely not that of a known clathrate cubic type because the 59 Bragg reflections of hydrate II do not fit properly with the cubic CS-I

or CS-II structure. The diffraction lines are even distinct from those of the (semi)clathrate CS-II.¹³ However, the hydrate II could well correspond to a composition of $\text{C}_2\text{H}_5\text{OH} \cdot (4.75–5)\text{H}_2\text{O}$ for which hydrates are known to decompose at $T_d \sim 198\text{ K}$.^{11,16}

The hydrate III of tetragonal structure could correspond to the stable hydrate $\text{C}_2\text{H}_5\text{OH} \cdot 2\text{H}_2\text{O}$ identified by Zelenin.¹⁶ This view is in accordance with the decomposition temperature ($T_d = 208\text{ K}$) and the domain of existence (concentration range) in the phase diagram.¹⁶

Finally, our hydrate I does not exist above $\sim 193\text{ K}$.²¹ Although most of the diffraction lines of hydrate I are compatible with the (semi)clathrate CS-I structure,¹³ the T_d of CS-I is different ($T_d \sim 208\text{ K}$). Our results further suggest the existence of hydrate I over a broad concentration range up to 42.5 mol %, ²¹ whereas the (semi)clathrate CS-I apparently exist only above $\sim 16\text{ mol \%}$.¹³

It should be noted that neither the metastable hydrate of $\text{C}_2\text{H}_5\text{OH} \cdot 3\text{H}_2\text{O}$ ($T_d = 204\text{ K}$) reported by Zelenin¹⁶ nor the (semi)clathrate CS-II reported earlier^{13,14,18} have been observed during our codeposition experiments (88 or 183 K). This discrepancy may be due to the distinct incorporation mechanism of EtOH molecules in ice. The structure of the solid formed certainly reflects the presence of clusters of distinctive structural nature with respect to those encountered in the vapor (during codeposition) or in the liquid (during freezing of aqueous solutions).

Atmospheric Implications. In the atmosphere, partial pressures of ethanol fluctuate. Phase diagrams of pressure–temperature type can be helpful and may help to explain variations in the structure formed. To our knowledge, such a diagram does not exist in the literature concerning the $\text{EtOH}–\text{H}_2\text{O}$ system. This diagram has been constructed from literature data and is represented in Figure 8. It displays the partial pressure of EtOH existing above ice at equilibrium as a function of temperature. The isosolubility curves are determined from Henry coefficients and the data of J. Timmermans.³⁹ Further, they are interpolated at low temperatures to determine the melting point of each composition.

The boundary that separates the different thermodynamic equilibrium areas (solid hydrate and solid solution regime) is materialized by the black main solid line in Figure 8. The crossed area located in the equilibrium area of ethanol solid solution in ice is representative of the EtOH atmospheric concentrations in the gas phase. We also plot the sublimation pressure curves of EtOH (open squares) and H_2O (solid squares).

At thermodynamic equilibrium, the ice vapor pressure is 7.10^{-5} Torr at 183 K.⁴⁰ Thus, the EtOH vapor pressures corresponding to the mixing ratios given in Table 1 vary between $P_{\text{EtOH}} \sim 4 \times 10^{-7}$ and $4 \times 10^{-5}\text{ Torr}$. Under these conditions and according to the equilibrium phase diagram, all samples investigated here are expected to fall within the solid solution regime where EtOH is extremely diluted in the ice matrix. Further, the lower bound is close to the atmospheric concentration value (Figure 8).

In contrast, from the mixing ratio and total pressure measurement in the reactor, the partial pressures of EtOH applied during deposition are estimated to vary between $5 \times 10^{-4}\text{ Torr}$ and $5.4 \times 10^{-2}\text{ Torr}$. This corresponds to relatively higher partial pressures of EtOH than those expected at thermodynamic equilibrium at 183 K. As can be seen in Figure 7, these points are all situated in the hydrate area of the phase diagram. Only

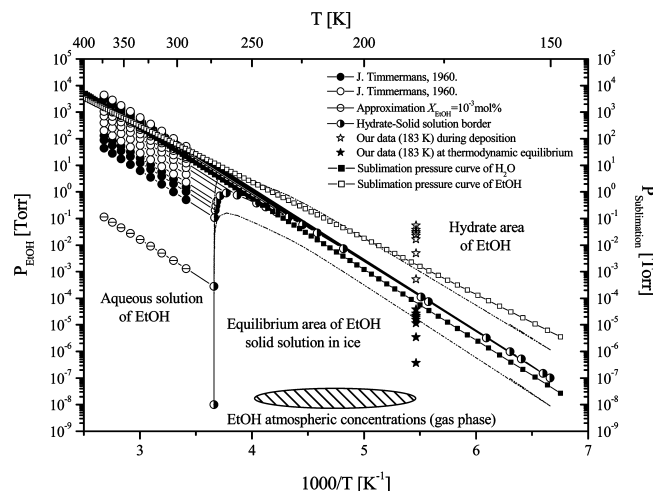


Figure 8. Equilibrium phase diagram of the EtOH–H₂O binary mixture; the partial pressure of EtOH at equilibrium above ice is plotted as a function of temperature. The solid and open squares symbolize the sublimation pressure curves of EtOH and ice, respectively. The stars represent our experimental measurements at 183 K. Solid stars correspond to partial pressures of EtOH expected at thermodynamic equilibrium using the mixing ratio of Table 1. Open stars correspond to partial pressures of EtOH applied during the codeposition. Iso-solubility curves (open and solid circles) are derived from literature data.³⁹ The iso-solubility curve at 10^{−3} mol % concentration is derived from Henry's law. The domain of existence of the solid solution regime is materialized by the main black solid line and the half-solid circles. It represents the equilibrium curve that separates the solid solution regime, the hydrate area, and the (ethanol aqueous solutions + gas) area.

one point (at low concentration) is found close to the boundary limit that separates the solid solution regime and the hydrate regime.

Our structural and Raman data reveal the formation of different hydrates during codeposition, which suggests that equilibrium is not reached during the incorporation of ethanol in ice by this mechanism. It seems likely that each new growth step of ice formed by deposition does not reach the equilibrium composition because the solid state diffusion of ethanol in ice is too slow to allow complete equilibration of each deposited ice layer.⁴¹ It thus seems reasonable to us to apply a condensation kinetic law rather than equilibrium to deduce the composition of the ice film.

In contrast, the solid mixture at $(X_{\text{EtOH}})_s = 0.3$ mol % falls within the confidence interval of the boundary line and may well correspond to the equilibrium area of EtOH solid solution in ice. This view is corroborated by our Raman results and the spectral features observed for EtOH diluted in ice (see discussion above and Figure 3). The properties (solubility of ethanol in ice) of this sample may now be transposed to the conditions occurring in the atmosphere.

Conclusion

Micro-Raman analysis and X-ray diffraction measurements have been performed on thin films obtained by the co-condensation of EtOH–water mixtures. Our results reveal the presence of two distinct ethanol hydrates, depending on the EtOH concentration. A first one (hydrate II), apparently stable between $(X_{\text{EtOH}})_s = 10.9$ and 18.8 mol % is reported. It is characterized spectroscopically by the presence of additional bands in the C–H vibrational mode spectral region. Its composition and temperature of decomposition ($T_d = 198$ K) could well correspond to the metastable hydrate C₂H₅OH·

(4.75–5)H₂O reported previously in frozen aqueous solutions^{11,16} and erroneously attributed to a clathrate CS-I.¹⁶ A distinct hydrate (hydrate III) is observed for $(X_{\text{EtOH}})_s \geq 22$ mol %. The diffraction results indicate that the structure is tetragonal with space group *P4/mmm*. On the basis of $T_d (= 208$ K), it is attributed to the stable hydrate of C₂H₅OH·2H₂O reported by Zelenin.¹⁶ At low EtOH content ($(X_{\text{EtOH}})_s = 0.3$ mol %), the Raman spectra reveal the existence of EtOH molecules extremely diluted in ice (solid solution). This regime can be transposed to conditions occurring in the troposphere. It is thus now conceivable to investigate the diffusion mechanism in ice (depth profiling) using Raman analysis under conditions relevant to the atmosphere.

Acknowledgment. The Centre d'Etudes et de Recherches Lasers et Applications is supported by the Ministère Chargé de la Recherche, the Région Nord-Pas de Calais and the Fonds Européen de Développement Economique des Régions. This research is supported in part by the national program "Les Enveloppes Fluides et l'Environnement" (LEFE) of the Centre National de la Recherche Scientifique.

Supporting Information Available: Additional information as noted in text. This material is available free of charge via the internet at <http://pubs.acs.org>.

References and Notes

- (1) Singh, H. B.; Kanakidou, M.; Crutzen, P. J.; Jacob, D. J. *Nature* **1995**, 378, 50.
- (2) Singh, H. B.; Chen, Y.; Staudt, A.; Jacob, D. J.; Blake, D.; Heikes, B.; Snow, J. *Nature* **2001**, 410, 1078.
- (3) Grosjean, E.; Rasmussen, R. A.; Grosjean, D. *Atmos. Environ.* **1998**, 32, 3371.
- (4) Kelly, T. J.; Callahan, P. J.; Plell, J.; Evans, G. F. *Environ. Sci. Technol.* **1993**, 27, 1146.
- (5) Fehsenfeld, F.; Calvert, J.; Fall, R.; Goldan, P.; Guenther, A. B.; Hewitt, C. N.; Lamb, B.; Liu, S.; Trainer, M.; Westberg, H.; Zimmerman, P. *Global Biogeochem. Cycles* **1992**, 6, 389.
- (6) Abbatt, J. P. D. *Chem. Rev.* **2003**, 103 (12), 4783.
- (7) Dominé, F.; Shepson, P. B. *Science* **2002**, 297, 1506.
- (8) Sokolov, O.; Abbatt, J. P. D. *J. Phys. Chem. A* **2002**, 106, 775.
- (9) Peybernès, N.; Le Calvé, S.; Mirabel, Ph. *J. Phys. Chem. B* **2004**, 108, 17425.
- (10) Kerbrat, M.; Le Calvé, S.; Mirabel, Ph. *J. Phys. Chem. A* **2007**, 111, 925.
- (11) Vuillard, G.; Satragno, N. *Compt. Rend.* **1960**, 250, 3841.
- (12) Potts, A. D.; Davidson, D. W. *J. Phys. Chem.* **1965**, 69, 996.
- (13) Boutron, P.; Kaufmann, A. *J. Chem. Phys.* **1978**, 68, 5032.
- (14) Takaizumi, K.; Wakabayashi, T. *J. Solution Chem.* **1997**, 26, 927.
- (15) Murthy, S. S. N. *J. Phys. Chem. A* **1999**, 103, 7927.
- (16) Zelenin, Y. M. *J. Struct. Chem.* **2003**, 44, 130.
- (17) Takamuku, T.; Saisho, K.; Nozawa, S.; Yamaguchi, T. *J. Mol. Liq.* **2005**, 119, 133.
- (18) Takaizumi, K. *J. Solution Chem.* **2005**, 34, 597.
- (19) Franks, F.; Desnoyers, J. *Alcohol–Water Mixtures Revisited*. In: *Water Science Reviews*; Franks, F., Ed.; Cambridge University Press: Cambridge, 1985, Vol. 1; p 171.
- (20) Chazallon, B.; Celik, Y.; Focsa, C.; Guinet, Y. *Vib. Spectrosc.* **2006**, 42, 206.
- (21) Chazallon, B.; Focsa, C.; Capet, F.; Guinet, Y. *Physics and Chemistry of Ice*; Kuhs, W. F., Ed.; Royal Society of Chemistry: Cambridge, UK, 2007, pp 133–140.
- (22) Chazallon, B.; Oancea, A.; Capoen, B.; Focsa, C. *Phys. Chem. Chem. Phys.* **2008**, 10, 702.
- (23) Chazallon, B.; Lebrun, N.; Dhamelincourt, P.; Toubin, C.; Focsa, C. *J. Phys. Chem. B* **2005**, 109, 432.
- (24) Altomare, A.; Caliendo, R.; Camalli, M.; Cuocci, C.; Giacomazzo, C.; Moliterni, A. G. G.; Rizzi, R. *J. Appl. Crystallogr.* **2004**, 37, 1025.
- (25) Wilson, G. J. *Am. Chem. Soc.* **1964**, 86, 127.
- (26) Gmehling, J.; Onken, U.; Rarey-Nies, J. R. *Liquid Equilibrium Data Collection*; Dechema Chemistry Data Series; Dechema: Frankfurt, 1977; Vol. I/2e.
- (27) Brown, D. E.; George, S. M. *J. Phys. Chem.* **1996**, 100, 4988.
- (28) Perchard, J. P.; Josien, M. L. *J. Chim. Phys.* **1968**, 65, 1834.
- (29) Perchard, J. P.; Josien, M. L. *J. Chim. Phys.* **1968**, 65, 1856.

- (30) Gan, W.; Zhang, Z.; Feng, R. R.; Wang, H. F. *Chem. Phys. Lett.* **2006**, *423*, 261.
- (31) Yu, Y.; Lin, K.; Zhou, X.; Wang, H.; Liu, S.; Ma, X. *J. Phys. Chem. C* **2007**, *111*, 8971.
- (32) Mizuno, K.; Miyashita, Y.; Shindo, Y. *J. Phys. Chem.* **1995**, *99*, 3225.
- (33) Gu, Y.; Kar, T.; Scheiner, S. *J. Am. Chem. Soc.* **1999**, *121*, 9411.
- (34) Hobza, P.; Havlas, Z. *Chem. Rev.* **2000**, *100*, 4253.
- (35) Oliveira, B. G.; Vasconcellos, M. L. A. A. *J. Mol. Struct.: THEOCHEM* **2006**, *774*, 84.
- (36) Mizuno, K.; Imafuji, S.; Fujiwara, T.; Ohta, T.; Tamiya, Y. *J. Phys. Chem B* **2003**, *107*, 3972.
- (37) Loveday, J. S.; Nelves, R. J. *Phys. Chem. Chem. Phys.* **2008**, *10*, 937.
- (38) Davidson, D. W. In *Water. A Comprehensive Treatise*; Franks, F., Ed.; Plenum Press: London, 1972; Vol. 2; Chapter 3.
- (39) Timmermans, J. *The Physico-chemical Constants of Binary Systems in Concentrated Solutions*; Interscience Publishers, Inc.: New York, 1960, Vol. 4.
- (40) Marti, J.; Mauersberger, K. *Geophys. Res. Lett.* **1993**, *20*, 363.
- (41) Dominé, F.; Rauzy, C. *Atmos. Chem. Phys. Discuss.* **2004**, *4*, 4719.

JP101440Y